ADVANCED ENERGY MATERIALS
www.advenergymat.de

Ti-Gradient Doping to Stabilize Layered Surface Structure for High Performance High-Ni Oxide Cathode of Li-Ion Battery

Defei Kong, Jiangtao Hu, Zhefeng Chen, Kepeng Song, Cheng Li, Mouyi Weng, Maofan Li, Rui Wang, Tongchao Liu, Jiajie Liu, Mingjian Zhang, Yinguo Xiao,* and Feng Pan**

High-Ni layered oxide cathodes are considered to be one of the most promising cathodes for high-energy-density lithium-ion batteries due to their high capacity and low cost. However, surface residues, such as NiO-type rock-salt phase and Li_2CO_3, are often formed at the particle surface due to the high reactivity of Ni^{3+}, and inevitably result in an inferior electrochemical performance, hindering the practical application. Herein, unprecedentedly clean surfaces without any surface residues are obtained in a representative $LiNi_{0.8}Co_{0.2}O_2$ cathode by Ti-gradient doping. High-resolution transmission electron microscopy (TEM) reveals that the particle surface is composed of a disordered layered phase (≈6 nm in thickness) with the same rhombohedra structure as its interior. The formation of this disordered layered phase at the particle surface is electrochemically favored. It leads to the highest rate capacity ever reported and a superior cycling stability. First-principles calculations further confirm that the excellent electrochemical performance has roots in the excellent chemical/structural stability of such a disordered layered structure, mainly arising from the improved robustness of the oxygen framework by Ti doping. This strategy of constructing the disordered layered phase at the particle surface could be extended to other high-Ni layered transition metal oxides, which will contribute to the enhancement of their electrochemical performance.

1. Introduction

With the great demands in Li-ion batteries' application for electric vehicles and grid-level energy storage, high-Ni layered oxides, $LiNi_xCo_yMn_zO_2$ ($x + y + z = 1$, $x \geq 0.7$), are considered as one of the most promising cathodes to meet the requirement for high-energy density application due to the high theoretical capacity (around 280 mA h g^{-1}) and low cost.[1] However, the poor cycling stability is a major drawback hindering its commercial application. Lots of efforts have been devoted to reveal the origin of the low cycling stability and improve its cycling performance. It is known that NiO-type rock-salt phase and Li_2CO_3 residue are two kinds of commonly-observed surficial species.[2] Both of these two substances are electrochemically inactive and poor in electronic and ionic conductivity, thus leading to high impedance to Li^+ (de)intercalation during cycling.[3] A significant power fade, up to 43%, was reported in $LiNi_{0.8}Co_{0.2}O_2$ due to the formation of NiO-type rock-salt phase on the particle surface.[4] It was also reported that NiO-like rock-salt phase and Li_2CO_3 formed on the surface of primary particles accelerate cracking in the secondary particles and eventually lead to the capacity fade with cycling.[5] Moreover, Li_2CO_3 on the particle surface was recently revealed to be the main source of CO_2 and CO generated during the first charge, and it reacts with electrolyte and produce LiF and other gases at high voltages, consequently causing impedance increase, capacity and power fading,

D. Kong, Dr. J. Hu, Z. Chen, M. Weng, M. Li, R. Wang, T. Liu, J. Liu, Dr. M. Zhang, Dr. Y. Xiao, Prof. F. Pan
School of Advanced Materials
Peking University
Shenzhen Graduate School
Shenzhen 518055, P. R. China
E-mail: zhangmj@pkusz.edu.cn; y.xiao@pku.edu.cn; panfeng@pkusz.edu.cn
Dr. K. Song
Shenyang National Laboratory for Materials Science
Institute of Metal Research
Chinese Academy of Sciences
Shenyang, Liaoning 110016, P. R. China
C. Li
Jülich Centre for Neutron Science
Forschungszentrum Jülich GmbH Outstation at Spallation Neutron Source (SNS)
Oak Ridge, TN 37831-6473, USA
Dr. M. Zhang
Sustainable Energy Technologies Department
Brookhaven National Laboratory
Upton, NY 11973, USA
The ORCID identification number(s) for the author(s) of this article can be found under https://doi.org/10.1002/aenm.201901756.

DOI: 10.1002/aenm.201901756

and even electrode swelling.[6] In brief, NiO-like rock-salt phase and surficial Li_2CO_3 impurity at the particle surface, generated from the surface side reactions between the high reactive Ni^{3+} with CO_2/H_2O in air, have been identified as the main reasons for the poor surface stability of high-Ni layered oxides. Hence, it is significant to develop new strategies to eliminate these surface residues and to construct an electrochemically-favored surface for high-Ni layered cathode materials.

In order to solve the problem of surface instability, lots of methods have been adopted previously, such as washing,[7] surface coating (ZnO, Al_2O_3, Li_2ZrO_3, Li_3PO_4, Li_xAlO_2, $Li_xTi_2O_4$),[1b,8] elemental doping, and constructing core–shell and concentration-gradient nanostructures (Ni-rich inside and Mn-rich outside).[9] Elemental doping, such as Al^{3+}, Zr^{4+}, Mn^{4+}, etc.,[1a,10] has been considered as an effective way to implement the surface protection. Taking Mn^{4+} as an example, Mn^{4+} ions bring with a shorter and stronger Mn—O bond than Ni/Co—O bonds, resulting in stable transition metal (TM) layers. Meanwhile, the concentration of the highly-reactive Ni^{3+} at the particle surface decreases due to the charge balance of Mn^{4+} and Ni^{2+}. Consequently, the amount of Ni^{2+} increases and results in more Li/Ni antisites at the particle surface, stabilizing Li layers during Li insertion/extraction.[11] The strategy of constructing Mn-rich surface, including core–shell and concentration-gradient structure,[9] can also effectively protect the particle surface of high-Ni layered oxides, and deliver excellent electrochemical performance. Nevertheless, such doping strategy could not completely prevent the formation of the detrimental surficial residues, including rock-salt phase and Li_2CO_3 at the particle surface.[1a,10,12] Similar to Mn^{4+}, Ti^{4+} represents another transition metal ion with valence state of 4^+, which has been extensively adopted as an effective dopant to improve the electrochemical performance.[13] However, the structural origin for the enhanced performance has never been clearly illustrated.

Herein, we construct a clean surface without any surficial residues via Ti-gradient doping in a representative high-Ni layered oxide $LiNi_{0.8}Co_{0.2}O_2$. In comparison with the undoped counterpart, it delivers a much improved electrochemical performance, including an extended life at high upper cutoff voltage (4.5 V) and high temperature (45 °C), as well as the best rate performance (146 mA h g^{-1}) at a high rate (20C). The spherical aberration correction transmission electron microscopy (TEM) reveals that a layered phase with serious cationic mixing is located at the near-surface region with the thickness about 6 nm. First-principles calculations further confirm that, the excellent electrochemical performance originates from the great chemical/structural stability of such layered structure at the particle surface.

2. Results and Discussion

2.1. Formation of Ti-Gradient Doping

The structural phases of NC82 and NC82-Ti were examined by XRD as shown in Figure S1 in the Supporting Information. All diffraction peaks can be indexed with the rhombohedral structure and are consistent with the standard pattern of $LiNi_{0.8}Co_{0.2}O_2$ (PDF#87-1562), indicating the formation of the pure layered phase. The morphology of the precursor $Ni_{0.8}Co_{0.2}(OH)_2$ and the final samples NC82 and NC82-Ti are presented at Figure S2 in the Supporting Information. Obviously, the final materials are in the form of small particles with the particle size about 1–2 μm. N_2 adsorption/desorption isotherms are performed as shown in Figure S3 in the Supporting Information, the final area surface of NC82-Ti is 5.57 m^2 g^{-1}, which is higher than NC82 (1.99 m^2 g^{-1}). By taking advantage of high sensitivity of neutron to both Li and O atoms, neutron diffraction experiments are performed, and the neutron diffraction patterns of NC82 and NC82-Ti are presented in **Figure 1**a,b, respectively. The structural refinements are performed by using a layered structural model with/without Ti doping, and the structural refinement results are listed in Table S1 in the Supporting Information. It is revealed that, Li/Ni antisite concentration, represented by the occupancies of Ni at 3b sites (Ni(3b)) is rising up from 0.0133 to 0.0230 due to Ti doping. It could be understood as such, in order to realize charge balance, more Ni^{2+} are generated because of the introduction of Ti^{4+}, which facilitates the exchange between Li^+ and Ni^{2+} and result in more Li/Ni antisites in NC82-Ti. In addition, Li slab in NC82-Ti shows a negligible shrink (0.026%) after Ti doping, which will not affect the high Li^+ diffusivity in the layered framework.[14]

In order to clarify the Ti distribution within single particles in NC82-Ti, the EDX mapping on a cross-section sample of a single particle is performed by a spherical aberration correction TEM (Figure S4, Supporting Information). It is clear that, Ti doping is successfully implemented in the bulk of the single particle. The actual doping content of Ti is determined as 1.59% relative to transition metal by inductively coupled plasma atomic emission spectroscopy (ICP-AES) in Table S2 in the Supporting Information. In order to further study the Ti distribution at the particle surface, X-ray photoelectron (XPS) depth profile by ion etching, a unique surface-sensitive technique, is performed. As shown in Figure 1c, the Ti $2p_{2/3}$ peak gradually shifts to the low energy direction with the etching time, indicating the gradual decrease of the charge valence for Ti ($Ti^{4+} \rightarrow Ti^{3+}$), which may come from the reduction effect of the Ar^+ ion beam.[15] XPS spectra for Ni and Co are deposited in Figure S5 in the Supporting Information. Based on the XPS spectra, the relative content of Ti could also be deduced as a function of the etching time, in consideration of the uniform distribution of Ni and Co within single particle. As shown in Figure 1d, the relative content of Ti decreases gradually from 10% to 3% with increasing etching depth up to around 10 nm by adopting the etching rate for SiO_2 (0.07 nm s^{-1}) as reference, hinting that a gradient Ti concentration at the particle surface. Such a unique element distribution may bring with a unique microstructure at the very local surface, and eventually affect the electrochemical performance.

2.2. Clean Surface with a Li/Ni-Exchange Disordered Layered Phase

In considering of Ti-gradient doping on the particle surface revealed above, local structure, especially at the particle surface, is further analyzed for NC82 and NC82-Ti. As shown in **Figure 2**a,b, the high resolution TEM (HRTEM) images of NC82 and NC82-Ti are demonstrated. NC82 exhibits a coarse

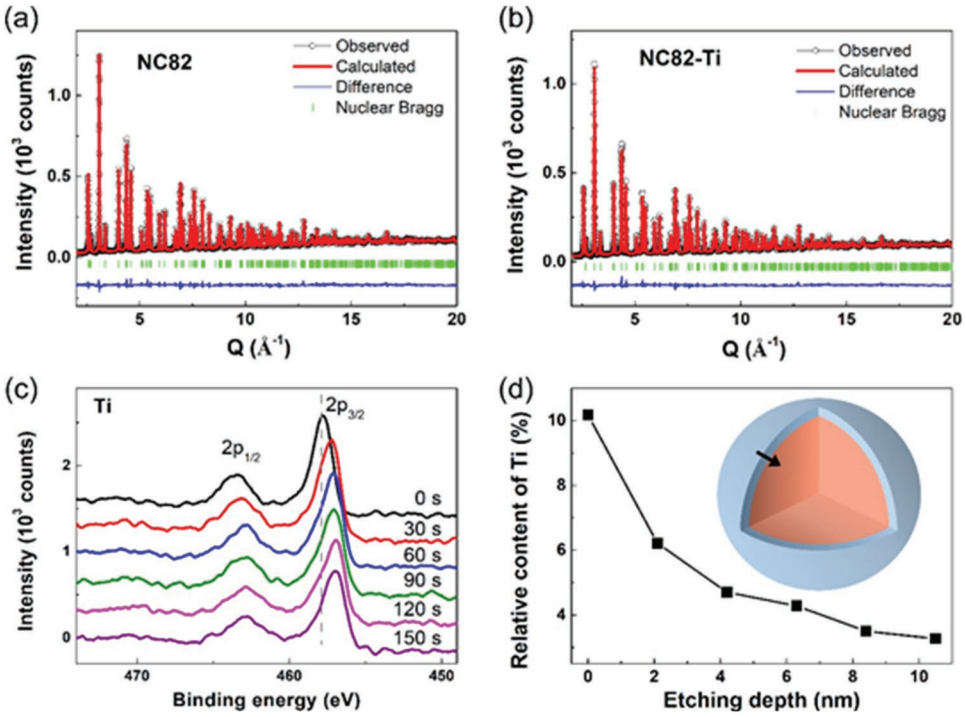

Figure 1. The structural determination and Ti doping. The neutron powder diffraction data of NC82 a) and NC82-Ti b). c) XPS spectra for NC82-Ti at different etching levels. d) An illustration for the relative content of Ti as a function of the etching time based on (c), showing the Ti distribution from the surface to the bulk.

surface coated with a 6 nm thick rock-salt phase (Figure 2a), and it will block the Li^+ diffusion pathway to a great extent within the *ab*-plane. This phenomenon has been extensively reported as surface reconstruction in the previous works, and identified as an important reason for the gas release during 1st cycle and the poor cycling stability.[3–5] Unprecedentedly, NC82-Ti presents a continuous layered structure extending from the bulk to the outermost surface as illustrated in Figure 2b, and no secondary phase is observed at the particle surface. Such a clean surface with unique layered structure has never been reported previously. It would greatly benefit the Li^+ diffusion at the particle surface, and bring with the unique electrochemical performance.

To further illustrate the structural details at the particle surface of NC82-Ti, Figure 2c presents a spherical aberration correction TEM image for NC82-Ti. It is clear that, the surface region could be roughly divided into two parts as guided by the blue line. The atomic contrast in the Li layers becomes clear from the bulk to the surface along the yellow arrows across the blue line. It indicates that, a well-ordered layered structure with less Li/Ni antisites in the bulk gradually evolves into a disordered layered structure with more Li/Ni antisites in the very-near surface area of around 6 nm in thickness.[16] The comparison of FFT maps of the two chosen regions in Figure S6 in the Supporting Information could further confirm the structural change of cationic disordering at the particle surface. As shown in Figure S7 in the Supporting Information, two HRTEM images with larger views recorded from different primary particles of NC82-Ti demonstrate that, the clean surface with the disordered layered region is statistically true. The formation of the unique surface structure should be attributed to the Ti^{4+}-gradient doping at the particle surface.

2.3. Electrochemical Performance

To evaluate the effects of the unique layered-structure surface on the electrochemical performance, NC82 and NC82-Ti are assembled into half coin cells with lithium foils as anodes for the measurement of their electrochemical performance. The cyclic voltammetry (CV) curves, which mostly manifest the reactivity of particle surface, are first performed for two samples. The oxidation/reduction main peaks in 1st and 2nd cycles for NC82 are around 4.00 and 3.60 V, respectively, indicating a big polarization between the oxidation section and the reduction section (**Figure 3**a). In contrast, the main peaks for NC82-Ti sample both located at 3.70 V in Figure 3b, implying a negligible polarization. With the increase of cycling numbers, all the oxidation peaks shift to the low potential for two samples, indicating the occurrence of surface reconstruction reaction. Finally, in the 3rd cycle, the oxidation/reduction main peaks located around 3.65 and 3.70 V, showing similar CV curves for two samples. It indicates that, the surface reconstruction reaction is finally completed and reached a reversible electrochemical equilibrium at the particle surface. In brief, NC82-Ti undergoes an obvious small shift from the initial nonequilibrium state to the final equilibrium state in comparison with NC82, implying that the surface of NC82-Ti is much close to an ideal electrochemical surface. The deduction is further confirmed

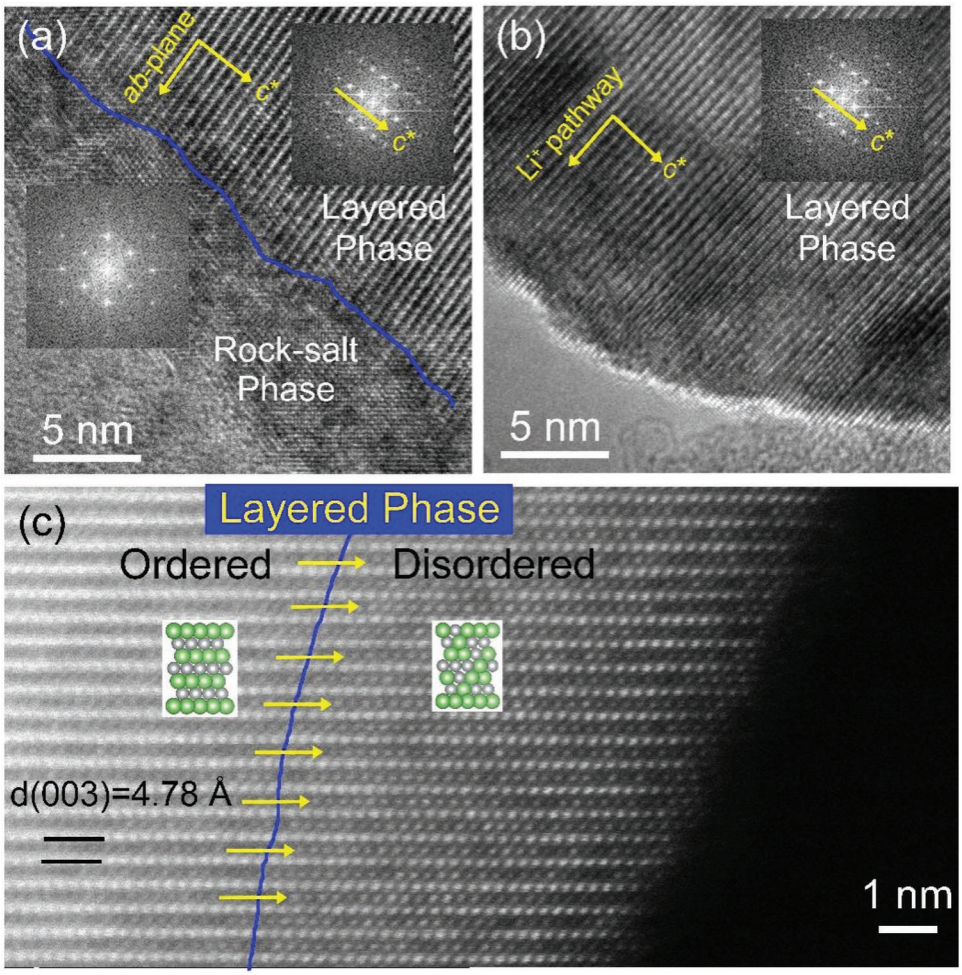

Figure 2. Clean surface with a disordered layered structure induced by Ti-gradient doping. The high-resolution TEM (HRTEM) images of as-prepared a) NC82 and b) NC82-Ti with FFT maps for different regions (insets). c) High-angle annular dark-field scanning TEM (HAADF-STEM) image of NC82-Ti by spherical aberration correction TEM. The green and grey balls represent Li^+ ions and TM cations, respectively.

by the sharper and more well-defined oxidation/reduction peaks observed in the dQ/dV curve of NC82-Ti than that of NC82 during the 1st cycle (Figure S8, Supporting Information). These results are consistent with predictions of electrochemical performance for NC82 with the rock-salt residues at the particle surface and for NC82-Ti with the clean surface as demonstrate clearly in Figure 2.

The rate performance for these two samples is further studied in the voltage range of 2.8–4.3 V (Figure 3c). The average discharge capacities of NC82-Ti and NC82 are similar, i.e., around 190 mA h g^{-1} at a low rate of 0.2C. With the continuous increase of the rate from 0.2C to 0.5C, 1C, 2C, 5C, 10C, and 20C, the average discharge capacities decrease for both samples, and the capacities of NC82 exhibit a much faster decrease than that of NC82-Ti. At 20C, the discharge capacity of NC82-Ti are around 146 mA h g^{-1}, about 77% of the capacity at 0.2C, which is much higher than that of NC82 (120 mA h g^{-1}). As far as we know, this is one of the best rate performance ever reported.[1a,17] It may partially come from the larger surface area (Figure S3, Supporting Information), the lower charge-transfer resistance demonstrated by the electrochemical impedance spectra (Figure S9, Supporting Information) and the higher Li^+ diffusivity derived by galvanostatic intermittent titration technique (GITT) (Figure S10 and Table S3, Supporting Information), which are both originated from the disordered layered phase at the particle surface.

Based on the above results, the cycling stability is also tested at 25 °C with the rate of 1C. As shown in Figure 3d, the capacity retention of NC82-Ti after 200 cycles is 97.71%, much higher than that (75.90%) of NC82. More coin cells are tested to prove the reliability in Figure S11 in the Supporting Information. When the upper cutoff potential is elevated to 4.5 V, NC82-Ti has a capacity retention of 86.38% after 100 cycles (Figure 3e), still higher than NC82 (69.13%). It indicates that NC82-Ti owns a more stable structure than NC82 to bear a higher cutoff voltage. Given that the working temperature is important to the battery health and life, we also test the samples at high temperature 45 °C (Figure 3f). NC82-Ti show superior cycle ability (96.37%) compared with NC82 (68.14%), showing a similar good cycling stability as 25 °C. The good cycling stability should be related with the enhanced thermal stability in pristine materials, even in the charged cathodes, which are

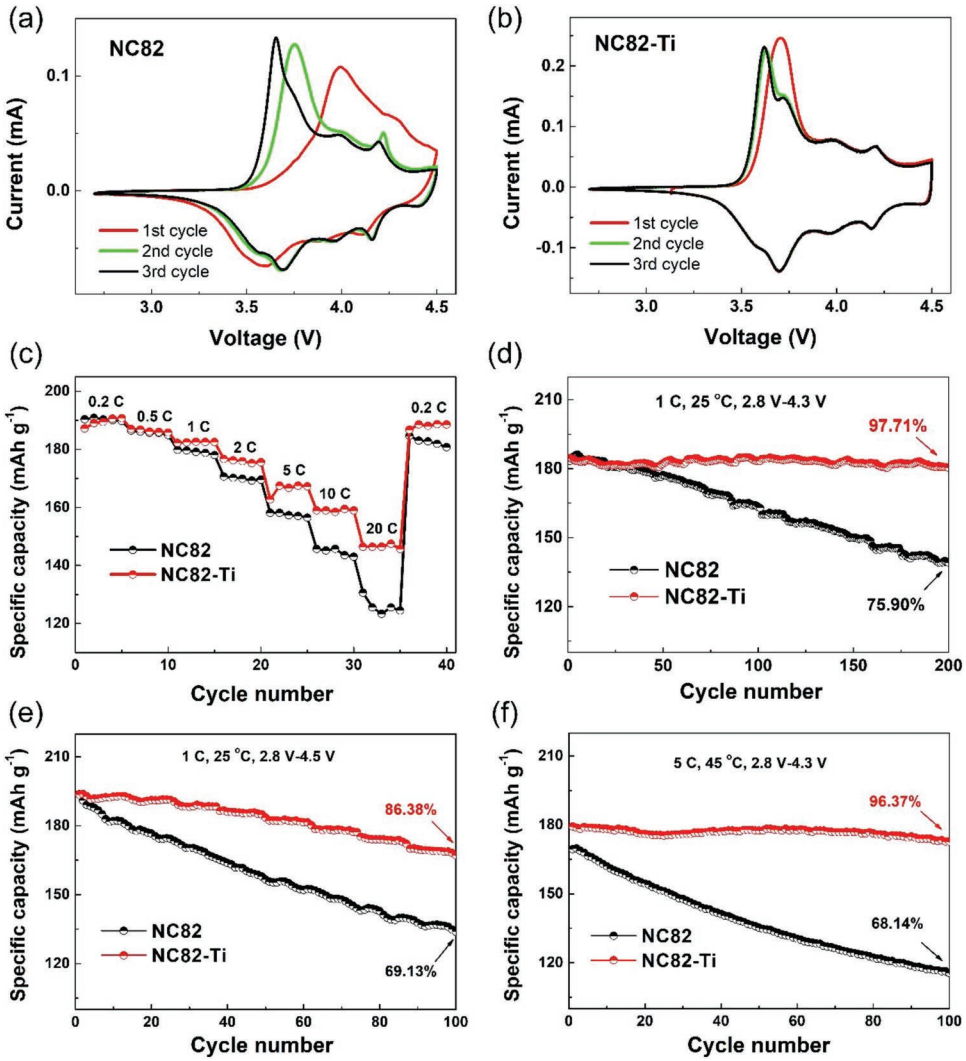

Figure 3. The electrochemical performance. The CV curves in the first 3 cycles for a) NC82 and b) NC82-Ti , measured between 2.7 and 4.5 V at a scan rate of 0.1 mV s^{-1}. c) The rate performance of NC82 and NC82-Ti in the voltage range of 2.8–4.3 V (1C = 200 mA h g^{-1}). The cycling stability of NC82 and NC82-Ti at 1C and 25 °C in the voltage range of d) 2.8–4.3 V and e) 2.8–4.5 V. f) The cycling stability of NC82 and NC82-Ti at 5 C and 45 °C in the voltage range of 2.8–4.3 V.

demonstrated by thermogravimetric analyzer (TGA) and Differential scanning calorimetry (DSC) measurements (Figure S12, Supporting Information). In addition, the storage performance is also evaluated. After aged in the air for 60 days, NC82-Ti also deliver a great capacity retention of 94.28% after 300 cycles at 1C (Figure S13, Supporting Information), which presents a superior storage performance.

In summary, the electrochemical performance, especially the rate performance and the cycling stability, are dramatically improved after Ti-gradient doping at the particle surface.

2.4. Ti Doping Induced Surface Stability by Theoretical Calculation

Why does Ti-gradient doping produce such a clean and air-stable surface, and lead to such excellent electrochemical performance? To answer this question, First-principles calculations are performed in consideration of both Ti doping and Li/Ni antisite observed above.

To explain the formation of disordered layered phase by Ti doping, the formation energies (ΔH_f) of three different models $LiNi_{1-x}Ti_xO_2$ with 1 Li/Ni antisite were calculated. These models shown in Figure S14 in the Supporting Information involve the pristine $LiNiO_2$, 8% Ti doping $LiNiO_2$, and 16% Ti doping $LiNiO_2$. The calculation results are listed in Table S4 and Figure S15 in the Supporting Information. As shown in Figure S15 in the Supporting Information, the curve goes down with the increase of x value. It indicates that, the formation energy decreases with Ti doping content, confirming the improved phase stability after Ti doping. The calculation results explain that why we obtain disordered layered phase at the particle surface after Ti doping.

To further validate the stability of this unique surface structure, we construct a $Li_{32}Ni_{32}O_{64}$ surface along the (104) direction based on a pure layered $LiNiO_2$ (O3 phase) in **Figure 4**a.[18]

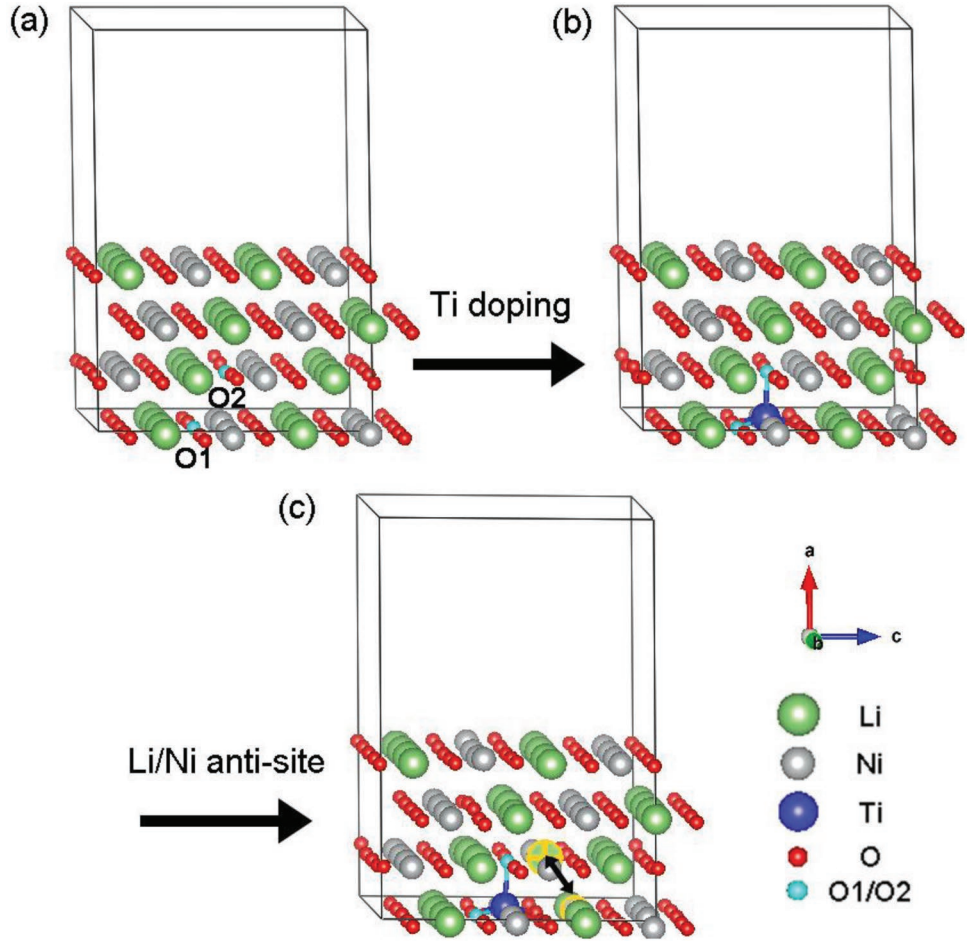

Figure 4. The structural models for first-principles calculations to investigate the effects of Ti-doping on the surface stability. a) $Li_{32}Ni_{32}O_{64}$ surface constructed along the (104) direction based on pure $LiNiO_2$, along with a vacuum slab of 10 Å. b) $Li_{32}Ni_{31}TiO_{64}$ surface after the doping of one Ti atom based on (a). c) $Li_{32}Ni_{31}TiO_{64}$ surface after introducing one Li/Ni antisite around the Ti atom based on (b). Li/Ni antisite is marked with a double-headed arrow. Two O atoms, O1 at the surface and O2 in the interior (marked by two cyan atoms), are chosen to calculate their binding energies.

Two oxygen atoms on the surface (O1) and inside (O2) (O1 and O2, marked by cyan balls) are chosen to calculate their binding energies (E_b). Ti doping is introduced to construct the Ti-doping model in Figure 4b.[19] Furthermore, one Li/Ni antisite is constructed around Ti atom to get the new model in Figure 4c. The O binding energies after Ti doping and introducing Li/Ni antisite are also calculated to make a comparison. All the calculation results are summarized in **Table 1**. As we can see, the binding energies for both O1 and O2 increase after Ti doping, and further increase after introducing Li/Ni antisite. It indicates that, the oxygen atoms are much more difficult to dissociate from the surface after Ti doping, hinting a more stable O^{2-} anion framework.

All these results not only phenomenally explain why the perfect layered structure instead of rock-salt phase could form at the particle surface when synthesizing high-Ni layered oxides, but also exhibit the excellent electrochemical stability of high-Ni layered oxides. The similar strategy could be further extended to Li-rich layered oxides and significantly improve their surface stability, which has been demonstrated by a very recent report.[20]

2.5. Insights into the Effect of Ti Doping

The effect of Ti doping on high-Ni layered cathode is hotly debated over the years. Even in a very recent study, Ti doping into high Ni layered oxides was reported to lead excellent electrochemical performance by a spinel surface.[21] However, the in-depth understanding has not established. Herein, based on the comprehensive experimental and theoretical evidences above, the concern is eventually figured out.

According to the previous reports, the poor cycling stability of high-Ni layered cathodes always arises from the side reactions between the high reactive Ni^{3+} and the electrolyte. Similarly, the poor storage property is also closely related with

Table 1. The binding energies (E_b) of O1 and O2.

	E_b(O1) [eV]	E_b(O2) [eV]
$Li_{32}Ni_{32}O_{64}$	1.78	1.16
$Li_{32}Ni_{31}TiO_{64}$	2.09	2.95
$Li_{32}Ni_{31}TiO_{64}$ (antisite)	2.75	3.03

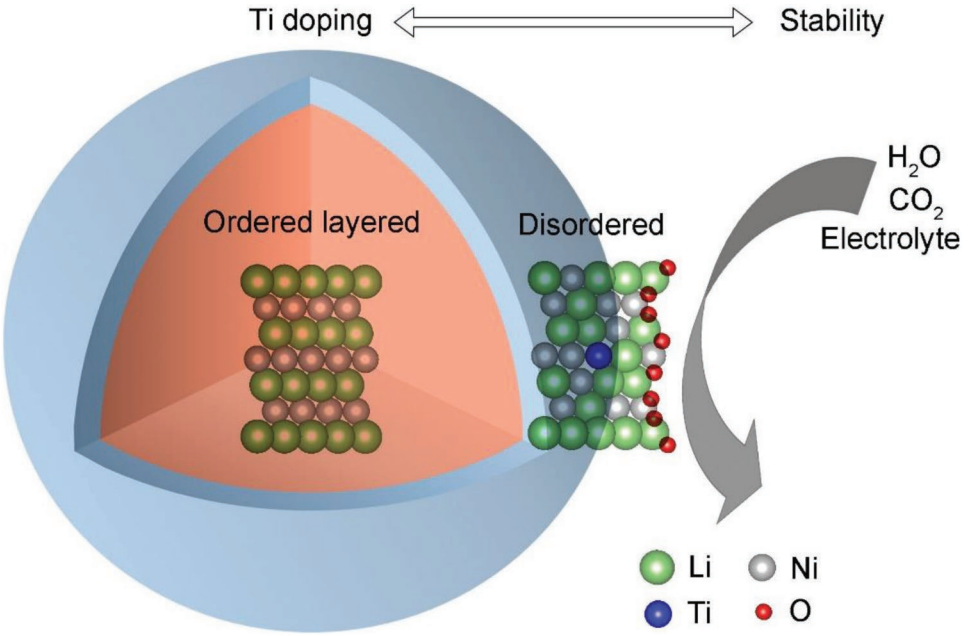

Figure 5. Schematic illustration to show the mechanistic understanding for Ti doping to enhance the storage/cycling stability. A disordered layered phase was constructed at the particle surface by Ti doping, greatly increasing the robustness of the oxygen framework, thereby resisting the corrosion of H_2O, CO_2, and electrolyte.

the side reaction between the high Ni^{3+} and H_2O/CO_2 in the air. As shown in **Figure 5**, Ti^{4+} doping decreases the content of Ni^{3+} due to the charge balance and induce more Li^+/Ni^{2+} mixing. This constructs a unique disordered layered structure at the particle surface, in contrast to the ordered layered structure in the bulk. More importantly, the binding energy of oxygen in such a disordered phase is significantly increased, especially on the surface. Therefore, the robustness of the oxygen framework at the particle surface is greatly boosted, which could effectively resist the corrosion of H_2O, CO_2, and electrolyte, even in the delithiated state.

3. Conclusion

In conclusion, an unprecedented clean surface with Li/Ni exchange disordered layered structure is constructed by Ti-gradient doping in a representative high-Ni layered oxide, $LiNi_{0.8}Co_{0.2}O_2$. It exhibits superior electrochemical performance in comparison with the undoped $LiNi_{0.8}Co_{0.2}O_2$, including the highest rate capacity reported yet (146 mA h g^{-1} at 20C) and the excellent cycling stability (a capacity retention of 95.55% after 200 cycles at 1C and 25 °C, and 96.37% after 100 cycles at 1C and 45 °C). Moreover, First-principles calculations reveal that, the excellent electrochemical performance originates from the great chemical/structural stability of disordered layered structure, which arises from the improved robustness of oxygen framework, especially at the surface. This strategy could be extensively applied to high-Ni layered oxides with different TM compositions, and expedites the steps into their commercialization for various high energy applications, especially for electric vehicles.

4. Experimental Section

Synthesis of $Ni_{0.8}Co_{0.2}(OH)_2$ Precursor: The hydroxide precursor $Ni_{0.8}Co_{0.2}(OH)_2$ was synthesized by the coprecipitation method. The whole reaction proceeded in a 10 L continuous stirred tank reactor (CSTR). Three kinds of solutions were prepared, 1 M mixed solution of $NiSO_4{\cdot}6H_2O$ and $CoSO_4{\cdot}7H_2O$ with a molar ratio of 4:1 (Solution I), 1 M NaOH and 1–1.5 M NH_4OH mixed solution with the same volume as solution I (Solution II) and 2 M NaOH solution (Solution III). First, 4 L of deionized water was added into the CSTR, and was kept at 55 °C. Second, Solution I and Solution II were dropped into the above solution with the same rate, and the pH value was controlled at around 10 by adding Solution III. After Solution I and Solution II were exhausted, the mixed solution in CSTR was kept at 55 °C with the stirring speed 600 rpm for 6 h. Finally, the products were filtered and washed by water for several times until the pH value of the filtrate was close to 7. The filtered product was dried at 120 °C for 10 h, then the greenish precursor $Ni_{0.8}Co_{0.2}(OH)_2$ was obtained.

Synthesis of $LiNi_{0.8}Co_{0.2}O_2$ and Ti-Doped $LiNi_{0.8}Co_{0.2}O_2$: $Ni_{0.8}Co_{0.2}(OH)_2$ precursor and $LiOH{\cdot}H_2O$ (98%, Aladin) were mixed together with a molar ratio of 1:1.06 and transferred into a mill pot, then a certain amount of alcohol was dropped. The mixture was ball milled with a constant rotate speed of 400 r min^{-1} for 4 h. The above mixture was blended with TiO_2 nanoparticles with Ti/TM molar ratios of (Ti/TM = 0 and 1.6%). Then it was sintered at 480 °C for 3 h, followed by 750 °C for 12 h in O_2 with a heating rate of 5 °C min^{-1}. The synthesis procedure of undoped $LiNi_{0.8}Co_{0.2}O_2$ followed the similar procedure. $LiNi_{0.8}Co_{0.2}O_2$ without and with Ti doping, are denoted as NC82 and NC82-Ti, respectively.

Material Characterization: The crystallographic structures of the samples were investigated by both X-ray and neutron diffraction measurements. The X-ray diffraction (XRD) patterns were collected using a Bruker D8 ADVANCE diffractometer with Cu *Kα* radiation. Neutron powder diffraction (NPD) experiments were performed on the time-of-flight neutron powder diffractometer POWGEN at the Spallation Neutron Source of Oak Ridge National Laboratory, USA. The diffraction profiles were analyzed with the Rietveld Refinement method with the Fullprof program suite. N_2 adsorption/desorption isotherms were performed on ASAP 2020. The morphological images of the final materials were

collected by scanning electron microscope (SEM, ZEISS Supra-55). The ingredients of the final samples were characterized by ICP-AES (JY2000-2). The thermal stability of NC82 and NC82-Ti was examined with a TGA (TGA/DSC1, Mettler Toledo) from room temperature to 1100 °C at a heating rate of 10 °C min^{-1} under N_2 flow. DSC measurement of charged materials was performed using a DSC 200 PC (Netzsch, Germany) at a temperature scan rate of 5 °C min^{-1}. For DSC analysis, the coin-cells were charged at a constant voltage of 4.3 V versus Li/Li^+ (2nd cycle) after 1st charging and discharging, and disassembled in an Ar-filled dry box. After carefully removing the remaining electrolyte solution from the surface of the electrode, the cathode materials were recovered from the current collector. An aluminum pan was used to collect 3.0 mg of samples. X-ray photoelectron spectra (ESCALAB 250XL) were also carried out to analyze the chemical states of the relevant elements. Ni 2p, Co 2p, C 1s, O 1s, and Ti 2p XPS spectra were measured with the corresponding exposure time as 10, 10, 20, 30, and 10 s, respectively. Etching time was 30 s, and the number of etching cycles is 5 times. After each etching cycle, the corresponding elemental XPS spectra would be taken once. The first C ls spectra before etching is used to calibrate all the other spectra, and the peak position of C-C peak in C 1s spectra is calibrated to 284.8 eV. The cross sectional samples were prepared by Ultrathin Slice Cutter (Leica UC7). Then they were characterized by a JEOL-3200FS high-resolution field-emission transmission electron microscopy (FETEM, 300 kV), and a FEI Titan 80–300 analytical TEM, 300 kV, with Cs-probe corrector and monochromator. Especially for the ex situ XPS and HRTEM measurements, the sintered samples were stored in a glovebox filling with N_2. It took about 1 h to take them out from the glovebox and be well prepared for the corresponding measurements.

Electrochemical Test: As-prepared materials, NC82 and NC82-Ti, were blended with acetylene black and polyvinylidenedifluoride (PVDF) with a weight ratio of 8:1:1 in *N*-methylpyrolidone (NMP). After stirring for 6 h, the formed slurry was coated on aluminum foil and dried in vacuum drying oven, which was punched into working electrodes with Arthe diameter 10 mm. Lithium metal foil and celgard 2502 membrane were regarded as the counter electrode and the separator. The ingredients of the electrolyte were 1 M $LiPF_6$ dissolved in ethylene carbonate (EC), diethyl carbon (DEC), and dimethyl carbonate (DMC) mixture with a volume ratio of 1:1:1. The coin cells were assembled in an argon-filled glove box. Galvanostatic discharge/charge tests were carried out in a NEWARE battery cycler at different temperatures. The CV were tested by a CHI 604E. GITT was measured by Moccor test cabinet between 2.7 and 4.35 V.[22] The electrochemical impedance spectra (EIS) were also carried out.

First-Principles Calculations: All calculations were performed using the PWmat code, which is a plane wave pseudopotential package based on density functional theory (DFT) accelerated by GPU architecture.[23] The Perduew–Bruke–Ernzerhof (PBE) form of global gradient approximation (GGA) was chosen as the exchange-correlation potential.[24] The spin = 2 polarization was used in all the calculations. The electron wave functions were expanded by plane waves with cutoff energies of 60 Ryds (816 eV), and the convergence tolerance for residual force and energy on each atom during structure relaxation were set to 0.01 eV $Å^{-1}$ and 10^{-5} eV, respectively. The vacuum space was set as 10 Å to avoid the interaction between periodical images. The Hubbard U (DFT + *U*) treatment was used on the transition metal. The *U* values for Ni and Ti were set to 6.4 and 1.9 eV following the literature values.[25]

The formation energy of $LiNi_{1-x}Ti_xO_2$ ($x = 0$, 0.08, and 0.16) is defined as the equation below

$$\Delta H_f = E_{tot}^{LiNi_{1-x}Ti_xO_2} - E_{crystal}^{Li} - (1-x)\,E_{crystal}^{Ni} - xE_{crystal}^{Ti} - E_{gas}^{O_2}$$

The binding energies of O atoms (denoted as E_b(O)) are calculated based on the following formula

$$E_b(O) = E'_{tot} + E(O) - E_{tot}$$

wherein, E_{tot} and E'_{tot} represent the total energies of the system before and after losing one oxygen atom. and E(O) represents the total energy of single isolated O atom.

Supporting Information

Supporting Information is available from the Wiley Online Library or from the author.

Acknowledgements

D.K. and J.H. contributed equally to this work. This work was financially supported by Guangdong Key-lab Project (Grant No. 2017B0303010130) and Shenzhen Science and Technology Research (Grant No. ZDSYS201707281026184). A portion of this research used resources at the Spallation Neutron Source, a DOE Office of Science User Facility operated by the Oak Ridge National Laboratory.

Conflict of Interest

The authors declare no conflict of interest.

Keywords

disordered layered phase, high-Ni layered oxide, Li-ion batteries, stable surface, Ti-gradient doping

Received: June 1, 2019
Revised: September 6, 2019
Published online: September 23, 2019

[1] a) Y. You, H. Celio, J. Y. Li, A. Dolocan, A. Manthiram, *Angew. Chem., Int. Ed.* **2018**, *57*, 6480; b) Y. J. Lim, S. M. Lee, H. Lim, B. Moon, K. S. Han, J. H. Kim, J. H. Song, J. S. Yu, W. Cho, M. S. Park, *Electrochim. Acta* **2018**, *282*, 311; c) J. Y. Li, W. D. Li, Y. You, A. Manthiram, *Adv. Energy Mater.* **2018**, *8*, 1801957; d) W. Lee, S. Muhammad, T. Kim, H. Kim, E. Lee, M. Jeong, S. Son, J. H. Ryou, W. S. Yoon, *Adv. Energy Mater.* **2018**, *8*, 1701788; e) J. Y. Li, W. D. Li, S. Y. Wang, K. Jarvis, J. H. Yang, A. Manthiram, *Chem. Mater.* **2018**, *30*, 3101; f) S. Q. Shi, J. Gao, Y. Liu, Y. Zhao, Q. Wu, W. W. Ju, C. Y. Ouyang, R. J. Xiao, *Chin. Phys. B* **2016**, *25*, 018212.

[2] a) S. T. Myung, F. Maglia, K. J. Park, C. S. Yoon, P. Lamp, S. J. Kim, Y. K. Sun, *ACS Energy Lett.* **2017**, *2*, 196; b) F. Lin, I. M. Markus, D. Nordlund, T. C. Weng, M. D. Asta, H. L. L. Xin, M. M. Doeff, *Nat. Commun.* **2014**, *5*, 3529; c) W. D. Li, B. H. Song, A. Manthiram, *Chem. Soc. Rev.* **2017**, *46*, 3006; d) H. H. Ryu, K. J. Park, C. S. Yoon, Y. K. Sun, *Chem. Mater.* **2018**, *30*, 1155.

[3] a) A. M. Andersson, D. P. Abraham, R. Haasch, S. MacLaren, J. Liu, K. Amine, *J. Electrochem. Soc.* **2002**, *149*, A1358; b) G. V. Zhuang, G. Y. Chen, J. Shim, X. Y. Song, P. N. Ross, T. J. Richardson, *J. Power Sources* **2004**, *134*, 293.

[4] D. P. Abraham, R. D. Twesten, M. Balasubramanian, J. Kropf, D. Fischer, J. McBreen, I. Petrov, K. Amine, *J. Electrochem. Soc.* **2003**, *150*, A1450.

[5] D. J. Miller, C. Proff, J. G. Wen, D. P. Abraham, J. Bareno, *Adv. Energy Mater.* **2013**, *3*, 1098.

[6] S. E. Renfrew, B. D. McCloskey, *J. Am. Chem. Soc.* **2017**, *139*, 17853.

[7] X. H. Xiong, Z. X. Wang, P. Yue, H. J. Guo, F. X. Wu, J. X. Wang, X. H. Li, *J. Power Sources* **2013**, *222*, 318.

[8] a) K. Park, J. H. Park, B. Choi, J. H. Kim, S. G. Hong, H. N. Han, *Electrochim. Acta* **2017**, *257*, 217; b) L. J. Li, M. Xu, Q. Yao, Z. Y. Chen, L. B. Song, Z. A. Zhang, C. H. Gao, P. Wang, Z. Y. Yu, Y. Q. Lai, *ACS Appl. Mater. Interfaces* **2016**, *8*, 30879.

[9] a) Y. K. Sun, Z. H. Chen, H. J. Noh, D. J. Lee, H. G. Jung, Y. Ren, S. Wang, C. S. Yoon, S. T. Myung, K. Amine, *Nat. Mater.* **2012**, *11*, 942; b) Y. K. Sun, S. T. Myung, B. C. Park, J. Prakash, I. Belharouak, K. Amine, *Nat. Mater.* **2009**, *8*, 320.
[10] U. H. Kim, S. T. Myung, C. S. Yoon, Y. K. Sun, *ACS Energy Lett.* **2017**, *2*, 1848.
[11] G. Sun, X. C. Yin, W. Yang, A. L. Song, C. X. Jia, W. Yang, Q. H. Du, Z. P. Ma, G. J. Shao, *Phys. Chem. Chem. Phys.* **2017**, *19*, 29886.
[12] Y. Li, R. Xu, Y. Ren, J. Lu, H. M. Wu, L. F. Wang, D. J. Miller, Y. K. Sun, K. Amine, Z. H. Chen, *Nano Energy* **2016**, *19*, 522.
[13] a) M. W. Xiang, W. Tao, J. H. Wu, Y. Wang, H. Liu, *Ionics* **2016**, *22*, 1003; b) R. Du, Y. J. Bi, W. C. Yang, Z. Peng, M. Liu, Y. Liu, B. M. Wu, B. C. Yang, F. Ding, D. Y. Wang, *Ceram. Int.* **2015**, *41*, 7133.
[14] a) K. Kang, G. Ceder, *Phys. Rev. B* **2006**, *74*, 094105; b) J. Q. Zhao, W. Zhang, A. Huq, S. T. Misture, B. L. Zhang, S. M. Guo, L. J. Wu, Y. M. Zhu, Z. H. Chen, K. Amine, F. Pan, J. M. Bai, F. Wang, *Adv. Energy Mater.* **2017**, *7*, 1601266.
[15] a) Y. Sakai, S. Ninomiya, K. Hiraoka, *Surf. Interface Anal.* **2012**, *44*, 938; b) R. Simpson, R. G. White, J. F. Watts, M. A. Baker, *Appl. Surf. Sci.* **2017**, *405*, 79.
[16] a) Y. Zhao, J. T. Liu, S. B. Wang, R. Ji, Q. B. Xia, Z. P. Ding, W. F. Wei, Y. Liu, P. Wang, D. G. Ivey, *Adv. Funct. Mater.* **2016**, *26*, 4760; b) H. L. Zhang, B. M. May, J. Serrano-Sevillano, M. Casas-Cabanas, J. Cabana, C. M. Wang, G. W. Zhou, *Chem. Mater.* **2018**, *30*, 692.
[17] a) M. Dong, Z. Wang, H. Li, H. Guo, X. Li, K. Shih, J. Wang, *ACS Sustainable Chem. Eng.* **2017**, *5*, 10199; b) W. G. Zhao, J. M. Zheng, L. F. Zou, H. P. Jia, B. Liu, H. Wang, M. H. Engelhard, C. M. Wang, W. Xu, Y. Yang, J. G. Zhang, *Adv. Energy Mater.* **2018**, *8*, 1800297; c) J. Kim, H. Cho, H. Y. Jeong, H. Ma, J. Lee, J. Hwang, M. Park, J. Cho, *Adv. Energy Mater.* **2017**, *7*, 1602559; d) H. J. Noh, Z. H. Chen, C. S. Yoon, J. Lu, K. Amine, Y. K. Sun, *Chem. Mater.* **2013**, *25*, 2109.
[18] M. D. Radin, S. Hy, M. Sina, C. C. Fang, H. D. Liu, J. Vinckeviciute, M. H. Zhang, M. S. Whittingham, Y. S. Meng, A. Van der Ven, *Adv. Energy Mater.* **2017**, *7*, 1602888.
[19] S. Hao, N. Zhao, C. Shi, C. He, J. Li, E. Liu, *Ceram. Int.* **2015**, *41*, 2294.
[20] S. Liu, Z. P. Liu, X. Shen, W. H. Li, Y. R. Gao, M. N. Banis, M. S. Li, K. Chen, L. Zhu, R. C. Yu, Z. X. Wang, X. L. Sun, G. Lu, Q. Y. Kong, X. D. Bai, L. Q. Chen, *Adv. Energy Mater.* **2018**, *8*, 1802105.
[21] F. Wu, N. Liu, L. Chen, Y. F. Su, G. Q. Tan, L. Y. Bao, Q. Y. Zhang, Y. Lu, J. Wang, S. Chen, J. Tan, *Nano Energy* **2019**, *59*, 50.
[22] W. Weppner, R. A. Huggins, *J. Electrochem. Soc.* **1977**, *124*, 1569.
[23] a) W. L. Jia, J. Y. Fu, Z. Y. Cao, L. Wang, X. B. Chi, W. G. Gao, L. W. Wange, *J. Comput. Phys.* **2013**, *251*, 102; b) W. L. Jia, Z. Y. Cao, L. Wang, J. Y. Fu, X. B. Chi, W. G. Gao, L. W. Wang, *Comput. Phys. Commun.* **2013**, *184*, 9.
[24] a) F. Zhou, M. Cococcioni, C. A. Marianetti, D. Morgan, G. Ceder, *Phys. Rev. B* **2004**, *70*, 235121; b) J. P. Perdew, K. Burke, M. Ernzerhof, *Phys. Rev. Lett.* **1996**, *77*, 3865.
[25] a) L. Wang, T. Maxisch, G. Ceder, *Phys. Rev. B* **2006**, *73*, 195107; b) V. I. Anisimov, J. Zaanen, O. K. Andersen, *Phys. Rev. B* **1991**, *44*, 943; c) Z. P. Hu, H. Metiu, *J. Phys. Chem. C* **2011**, *115*, 5841.